Proceedings of Global Power and Propulsion Society
ISSN-Nr: 2504-4400
GPPS Chania22
18th–20th September, 2022

www.gpps.global

GPPS-TC-2022-0035

Turbulence Anisotropy Analysis at the Middle Section of a Highly Loaded 3D Linear Turbine Cascade Using Large Eddy Simulation

N. Fard Afshar, J. Deutsch, S. Henninger
Institute of Jet Propulsion and Turbomachinery
RWTH Aachen University
fard-afshar@ist.rwth-aachen.de
Aachen, Germany

D. Kožulović
Institute of Jet Propulsion
Bundeswehr University Munich
Munich, Germany

P. Bechlars
MTU Aero Engines AG
Munich, Germany

ABSTRACT

This study analyzes the flow over a three-dimensional linear low-pressure turbine cascade blade using large eddy simulation at Re=90 k. The computational model consists of one blade passage with periodic boundaries and synthetic turbulence is generated at the inlet of the domain. Various flow metrics, including isentropic Mach number distribution at mid-span and wake total pressure losses are compared with available experimental data and found to be in good agreement. A more detailed analysis of the turbulence with particular attention to the separation bubble region is subsequently presented. The analysis revealed that the turbulence is in a nearly two-component state very close to the wall region and gradually follows a certain anisotropy trajectory, as the distance from the wall increases. Even in the free-stream region no fully isotropic state is reached, due to large acceleration and flow turning. The results give a new insight into the state of turbulence within the separation region on the blade suction side and emphasize the deficiencies of the Reynolds-averaged Navier Stokes (RANS) turbulence models in reproducing the turbulence anisotropy. This insight is of relevance for the aerodynamic design of turbines, since large parts of the total pressure loss are generated in the separation region.

INTRODUCTION

According to Gier and Hübner (2005), low pressure turbines (LPT) are responsible for 30 % of the total weight and 15 % of the total engine cost. Hence, corresponding improvements yield significant benefit for the overall engine performance. Despite of long-term experience, the LPT design is still a challenging task due to increasing requirements on efficiency, weight, durability, manufacturing, maintenance, etc. One of the design trends is to decrease the LPT weight by reducing the number of blades. This results in the design principle of high-lift blades, which are subject to large adverse pressure gradients on the suction side. However, in the low Reynolds number regime, laminar boundary layer separation is likely and may be the primary cause of total pressure loss increase and corresponding efficiency decrease. In the case of non-reattached bubbles, the performance penalties are excessive, a situation wich has to be prevented. In order to maximize the blade loading and to assure a reattachment of the separation bubble, it is crucial that numerical design tools are sufficiently accurate to predict the correct reattachment.

The current state of computational fluid dynamics (CFD) for turbomachinery component design is based mainly on three-dimensional RANS methods, as these have a low turnaround time, while often providing satisfactory prediction accuracy. These methods are based on the temporal averaging of the flow equations for the Reynolds decomposed flow quantities in which all scales of turbulence, including transition, are modelled (Menter (1994), Wilcox (1988), Langtry and Menter (2009)). RANS turbulence models, in general, can be categorized into several classes. The most known classes are the linear eddy viscosity models (LEVM), explicit algebraic Reynolds stress models (EARSM) and differential Reynolds stress models (DRSM). LEVM are based on the Boussinesq assumption which relates the Reynolds stress tensor directly to the rate of strain tensor of the flow. DRSM, on the other hand, is considered as the most advanced RANS turbulence model. This concept originates from the work of Launder et al. (1975) and completely abandon the Boussinesq-hypothesis. EARSM

is obtained through a simplification of the DRSM, and can be perceived as an extension of LEVMs by including the non-linear relation between the turbulence stress tensor, the mean-flow gradient and the turbulence scales.

Despite the great efforts and the successes of recent decades, there is still a lack of prediction accuracy for challenging flow phenomena in turbomachinery (e.g. flow separation, transitional boundary layers, turbulence decay and complex turbulent structures). In particular, LPT's show significant deficiencies in RANS predictions, since - depending on varying Reynolds numbers (e.g. start or cruise) - different boundary layer states and transition mechanisms can occur (Denton (2010), Sandberg and Michelassi (2019)). While RANS methods are still the workhorse to perform extensive design variations, with the increase of computational power, high-fidelity simulations such as large eddy simulations (LES) can be performed for few selected operating points and designs. High-fidelity simulations facilitate the understanding of the complex 3D flow physics in the turbomachinery by providing deeper insight into the turbulence field. A profound understanding of the turbulence is necessary to advance the design of improved turbine and compressor blades.

Furthermore, several studies (Comte and Lesieur (1996), Huai et al. (1997)) have confirmed that accurate predictions of transition to turbulence are possible with the LES technique. Due to their reduced modeling share, LES can be mainly used in two ways: either for conducting design-of-experiment-like studies, which provide a thorough understanding of the physical aspects of turbomachinery flow; or for machine learning-based improvements of turbulence and transition models. One aspect of high-fidelity simulations that has not been extensively addressed in the literature is the wealth of information that resides in the anisotropy of the turbulent state. Theoretical methods have existed for a long time, but have not been fully exploited, including the anisotropy-invariant developed by Lumley (1979). Analyzing the anisotropy offers a different view on turbulence, revealing additional information not obviously observed in physical space. In the literature, there are some contributions on the turbulence anisotropy theory, focusing mainly on channel flow, turbulent boundary or wake flow (Fischer et al. (2001), Schenck and Jovanović (2002), Krogstad and Torbergsen (2000), Antonia et al. (1994)). The flow in turbomachinery has barely been investigated via anisotropy theories based on high-fidelity simulations in the past, with some exceptions focusing on compressor cascades (Yan et al. (2019)).

The present investigation aims to improve the understanding of various types of turbulence states by applying the anisotropy invariant theory to a wall-resolved LES (according to Tyacke and Tucker (2015)). For a modern high-lift LPT subject to a low Reynolds number flow regime the anisotropy of the turbulent state with focus on the attached laminar boundary layer, the free shear and the separation bubble are investigated in detail.

METHODOLOGY

Describing turbulence anisotropy

Any arbitrary turbulence state can be reconstructed by a linear combination of the three limiting turbulence states, namely: one-component (1C), isotropic two-component (2C), and isotropic (3C). Isotropic 3C turbulence, as the name suggests, forces the anisotropy to be zero, also called "spherical-shape" turbulence. Isotropic 2C turbulence represents a turbulence state in which only two fluctuating components of equal intensity exist ("pancake-shape" turbulence). In contrast, one-component turbulence (1C) is characterized by one fluctuating component which dominates over the other two (e.g. grid turbulence through axisymmetric expansion) and is called "cigar-shape" turbulence. Flows in engineering applications are usually strongly non-equilibrium and anisotropic due to boundaries and high adverse pressure gradients. Turbulence anisotropy can be quantified by the Reynolds stress anisotropy tensor a_{ij}, whose incompressible form is given by

$$a_{ij} = \frac{\overline{u_i' u_j'}}{2k} - \frac{\delta_{ij}}{3}\ , \quad k = \frac{\overline{u_i' u_i'}}{2} \tag{1}$$

where k is the turbulent kinetic energy and δ_{ij} the Kronecker delta. Lumley (1979) and Choi and Lumley (2001) used the invariants of a_{ij} and its constraints of realizability to visualize the state of turbulence. Banerjee et al. (2007) introduced a barycentric mapping by solving an eigenvalue problem of a_{ij}. The eigenvalues $\lambda_1 > \lambda_2 > \lambda_3$ are used to compute the weights C_{iC} of the linear combination of the three limiting turbulent states 1C, 2C and 3C. Thus, the anisotropy can be described by

$$a_{ij} = C_{1C} a_{1C} + C_{2C} a_{2C} + C_{3C} a_{3C} \tag{2}$$

with

$$C_{1C} = \lambda_1 - \lambda_2 \tag{3a}$$
$$C_{2C} = 2(\lambda_2 - \lambda_3) \tag{3b}$$
$$C_{3C} = 3\lambda_3 + 1 \tag{3c}$$

where a_{1C}, a_{2C} a_{3C} represent the Reynolds stress anisotropy tensors at the limiting turbulent states. To visualize the anisotropy, Emory and Iaccarino (2014) suggested assigning a unique color to each state in the barycentric map. This is achieved by mapping the weights C_{iC} of turbulent states to the RGB channels. The direct mapping of weight to channel

is shown in the top left corner of Figure 3b, with red assigned to 1C, green assigned to isotropic 2C and blue assigned to isotropic 3C.

Testcase

In this study, the highly loaded LPT profile MTU-T161 described by Gier et al. (2010) has been selected. Non-protected experimental as well as RANS (LEVM) and DNS simulation results were first published by Müller-Schindewolffs et al. (2017). The aerodynamic design point and the geometrical parameters of the LPT profile are given in Table 1.

Table 1 MTU-T161 profile classification

(a) Aerodynamic design point

Aerodynamic parameters	Values
$Re_{2,th}$	200,000
$Ma_{2,th}$	0.6
β_1	131.0°
β_2	25.0°
Zw	1.19

(b) Geometrical parameters

Geometrical parameters	Values
t/l	0.956
l	0.0699 m
β_s	61.72°
h_{LE}	0.1725 m
h_{TE}	0.1983 m

The three-dimensional model of the MTU-T161, including the diverging side walls, is shown in Figure 1a and the blade-to-blade view in Figure 1b. The profile has been investigated experimentally by Entlesberger et al. (2005) at the University of the Armed Forces in Munich. The measurements include inflow turbulence, profile pressure distribution and wake values. The measured freestream turbulence intensity of the cascade tunnel was increased by using a turbulence grid up to 9 %, decreasing to almost 3.5 % at the leading edge. The experimental results indicate a rapid increase in losses for Reynolds number below 120×10^3, as the laminar separation bubble on the suction side of the profile grows.

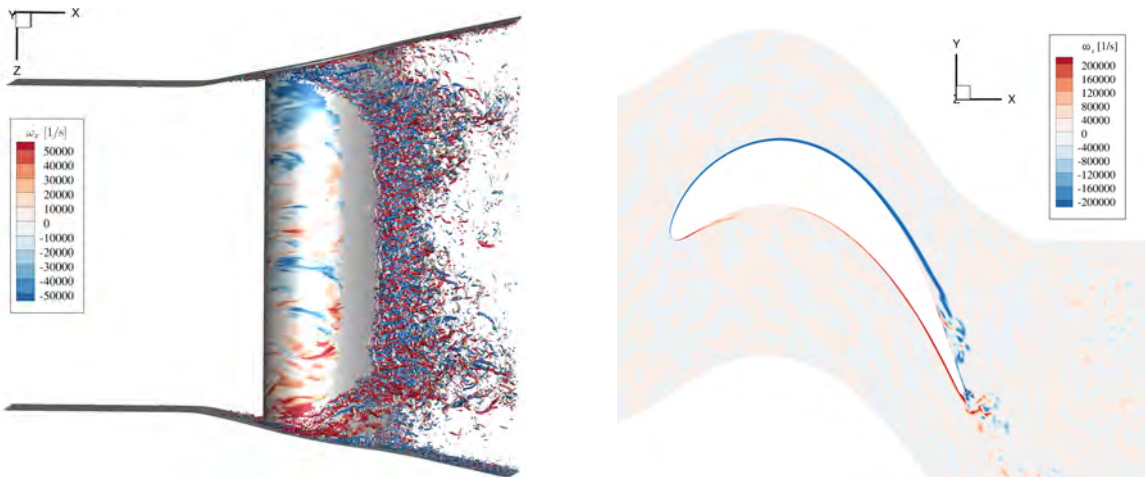

(a) 3D view of turbulent structures (isosurfaces of λ_2 criterion, colored by spanwise component of the vorticity)

(b) Blade cut at mid section colored by spanwise component of the vorticity

Figure 1 Instantaneous flow field for the MTU-T161 profile obtained by LES

Numerical Method

RANS (LEVM and DRSM) and LES calculations of the above 3D configuration were conducted using DLR's TRACE solver for turbomachinery flow simulation. TRACE has been used for LES of LPTS application in the past (Morsbach and Bergmann (2020), Leyh and Morsbach (2020)).

The LES calculations in TRACE solve the filtered compressible Navier-Stokes equations using a second-order accurate, density-based finite volume scheme applying MUSCL reconstruction (van Leer (1979)). LES uses a fraction of 1×10^{-3} of Roe's numerical flux (Roe (1981)), which is added to a central flux to avoid odd-even decoupling. The time integration is performed, in this case, using a third-order accurate explicit Runge-Kutta method. The subgrid stresses are computed by the WALE model developed by Nicoud and Ducros (1999).

A one-dimensional characteristic non-reflecting boundary condition implemented by Schlüß et al. (2016) is used at the domain outlet to drive the time- and surface-averaged boundary state towards the prescribed values (static pressure). For the simulation domain inlet, a Riemann boundary condition is applied to set the stagnation pressure, stagnation

temperature and flow angles. To reproduce realistic operating conditions, synthetic turbulent fluctuations in the inflow are introduced. The synthetic turbulence generator in TRACE uses the prescribed turbulent length scale and the Reynolds stress tensor components to represent the fluctuation field at the inlet based on superposition of Fourier modes (Shur et al. (2014)). These values are adapted from measurements such that the turbulent decay (from simulation inlet to leading edge) matches the experimental decay.
The LES grid consists of 85×10^6 nodes, with a normal wall resolution of $y^+ < 1$. The values of Δx^+ and Δz^+ are below 30 and 25 respectively, on the whole suction side. However, beginning at the accelerated laminar boundary layer close to the suction peak up to the trailing edge, the values of Δx^+ and Δz^+ are below 10, which assure a wall-resolved LES (Tucker (2014)). This is necessary for a detailed analysis of turbulence, especially in the near wall region.
The LES simulation is initialized using the k-ω solution. To avoid averaging over the initial transient phase, recording statistics is started after 10 convective time t_c, which is defined as

$$t_c = \frac{l_{ax}}{u_{ax,out}} \tag{4}$$

with an axial chord length $l_{ax} = 0.06\,\mathrm{m}$ and an approximate axial velocity at the domain outlet $u_{ax,out} \approx 77\,\mathrm{m/s}$. The start of the sampling period was chosen by evaluating several convergence criteria, such as acting forces on the blade surface, probe data at several locations, and analyzing the truncated mean-squared error, as described in Bergmann et al. (2022). After the initial transient is washed out, the statistics are accumulated for 40 convective times. This has been shown to be sufficient for a statistical convergence regarding the blade profile and wake values. The simulation has been conducted on a CPU system using Intel Skylake processors with a wall clock time of 336 hours on 1152 CPUs for 40 convective times.
The steady-state LEVM solution in this work was calculated by applying the k-ω turbulence model developed by Wilcox (1988), with the stagnation-point anomaly fix by Kato and Launder (1993), the γ-Re_Θ transition model developed by Langtry and Menter (2009) and a viscous blending technique described in Bode (2018) as an eddy viscosity limiter.
In order to extend the comparison, the hybrid SSG/LRR-ω differential Reynolds stress model developed in the EU-project FLOMANIA (see e.g. Eisfeld and Brodersen (2005); Eisfeld et al. (2016)) coupled with the γ-Re_Θ transition model of Langtry and Menter (2009) was used. Contrarily to the linear k-ω turbulence model which uses a constitutive relation to compute the Reynolds stresses based on Boussinesq's hypothesis, the SSG/LRR-ω full second-moment DRSM solves for each of the six Reynolds stresses a separate transport equation plus an additional transport equation for a variable determining the length scale. The basic idea of the SSG/LRR-ω model is to blend the ϵ-based SSG model (Speziale et al. (1991)) for regions of free shear flow with the LLR model (Launder et al. (1975)) near walls in the ω-based formulation. The model was chosen because in the solver TRACE only for this RSM a coupling with a transition model is available, which is necessary to capture the transition mechanism, separation and attachment.

RESULTS AND DISCUSSION

The following discussion is focused on the center plane of the cascade only, although the complete blade height together with the diverging endwalls was covered by the simulation. In this way, the 3D effects from the endwall regions are also accurately captured. These effects have a significant impact at midspan flow, especially due to the large endwall divergence.

Comparison to Experiment

Prior to a detailed investigation of the turbulence and anisotropy behaviour, the blade loading and the wake loss are evaluated and compared to the experimental results.

Figure 2a shows the isentropic Mach number (Ma_{is}) distribution, which is determined by the static pressure, around the profile. The LEVM results match very well with measurements at the leading edge, trailing edge and the aft pressure side. On the suction side, the Ma_{is}-distribution starts to deviate at $x/l_{ax} = 30\,\%$, where the simulation leads to larger Mach number and a shift of the suction peak downstream of the measured peak, from $x/l_{ax} = 60\,\%$ to $65\,\%$. Also the subsequent separation starts later than the measured one, but is much smaller and reattaches well before the trailing edge, at $x/l_{ax} = 90\,\%$. The DRSM results are almost identical to the LEVM results. Despite modelling the Reynolds stress separately and taking into account the transition via a transition model, there is no improvement considering the isentropic Mach number distribution. SSG/LRR-ω Reynolds-stress model uses a simple, linear model close to solid walls without any corrections. This might have a negative influence on representing the boundary layer state. In contrast, the LES simulation is in a much better agreement with the measurements, in particular at the suction peak and separation region. A similar situation is shown downstream the cascade at $x/l_{ax} = 1.4$, where LES predictions match the measured total pressure loss value very well, whereas the LEVM and DRSM simulations yield a thinner wake with a larger peak value.

The deficiencies of both RANS models to accurately predict the pressure distribution and the flow loss may be tracked back to the non-adequate reproduction of the turbulence effects in the separation and wake region. Since the separation point is in the laminar state, the turbulence is generated at the outer part of the separation bubble, where strongly

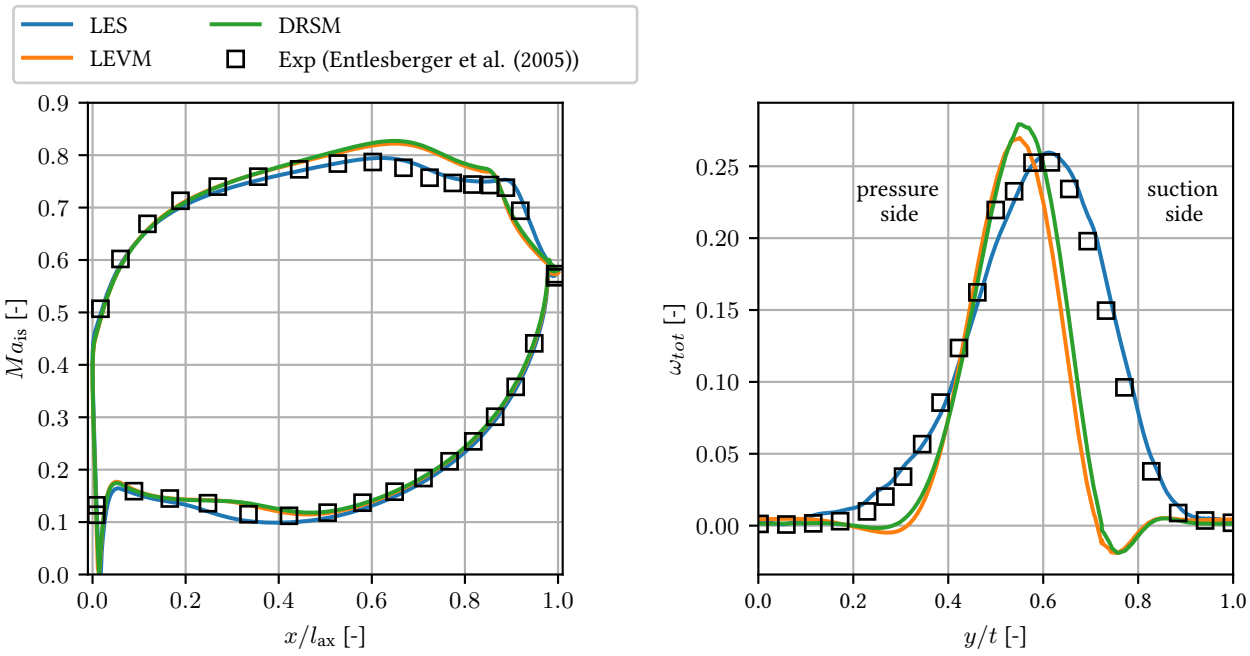

(a) Ma_{is} distribution at $50\,\%$ span **(b) Total pressure loss coefficient at $x/l_{ax} = 1.4$**

Figure 2 Comparison of averaged quantities of LES, LEVM, DRSM and experiment

anisotropic characteristics are present, as will be shown later. These characteristics are also propagated into the wake. The results of Figure 2 show that even DRSMs (SSG/LRR-ω in particular) have difficulties to capture the transition and separation bubble correctly. Such deficits have also been reported by Eisfeld et al. (2016) and Morsbach (2017). DRSMs offer improvements over the classical LEVMs and EARSMs when turbulence structure is considered. However, these improvements do not always extend to the mean flow quantities. Since the prediction of the boundary layer state and the modeling of the Reynolds stresses are some of the key parameters, the following sections of this paper will focus on a more detailed analysis based on anisotropy and the share of Reynolds stresses in the suction side boundary layer.

Separation and Transition to turbulence

It has been shown (Coull and Hodson (2011)) that two mechanisms dominate in LPT applications under elevated free stream turbulence (FST) conditions ($2\,\% - 3\,\%$ in the free stream and outer boundary layer in the current case). Firstly, the incoming turbulence interacts directly with Kelvin-Helmholtz (KH) rollers, leading to spanwise disturbances and subsequent breakdown. Secondly, the incoming turbulence accelerates the transition by creating turbulence spots in the initial part of the boundary layer. The transition is triggered by the development of the so-called Klebanoff streaks and a destabilized separated shear layer. Several authors argue that the KH instability plays a dominant role in the transition process of separation bubbles, whereas other experimental studies claim the Tollmien-Schlichting waves to be more significant (Volino (2010), Rist et al. (2004), Roberts and Yaras (2003), Yang (2011)).

To facilitate further discussion, a body-fitted coordinate system is introduced for the suction side region of the profile, with coordinate s starting from leading edge running to trailing edge and coordinate t representing the wall normal direction (Figure 3a). As such, we performed a transformation to the new coordinates for the region of interest on the suction side. In this area, velocities and Reynolds stresses are transformed to the new coordinate system where the indices 1, 2 and 3 indicate the wall parallel, wall normal and spanwise direction. t_{max} characterizes the edge of the wall normal coordinat t.

The suction side boundary layer around the MTU-T161 is characterized by the separation-induced transition mode. As shown in Figure 3a, the suction side boundary layer separates at around $x/l_{ax} = 0.61$ (region ①). As a consequence, the transition is triggered and completed in the aft section of the suction side, reaching a full turbulent state. This is supported by the maximum values of turbulent kinetic energy (TKE) shown at the bottom of Figure 3a (region ②). The maximum shear line ($\max(\partial u_1/\partial t)$) right above the separation bubble highlights the trajectory of the high TKE values. For the same geometry and operating point, Müller-Schindewolffs et al. (2017) showed that the laminar separation bubble causes an intensive Kelvin–Helmholtz instability, leading to the transition and the reattachment of the bubble.

Nevertheless, the main focus of the current work is not to discuss the prevailing transition mechanism in detail, but rather to demonstrate and analyze the turbulence anisotropy behavior of the suction side boundary layer (including separation

bubble, shear layer and reattachment regions).

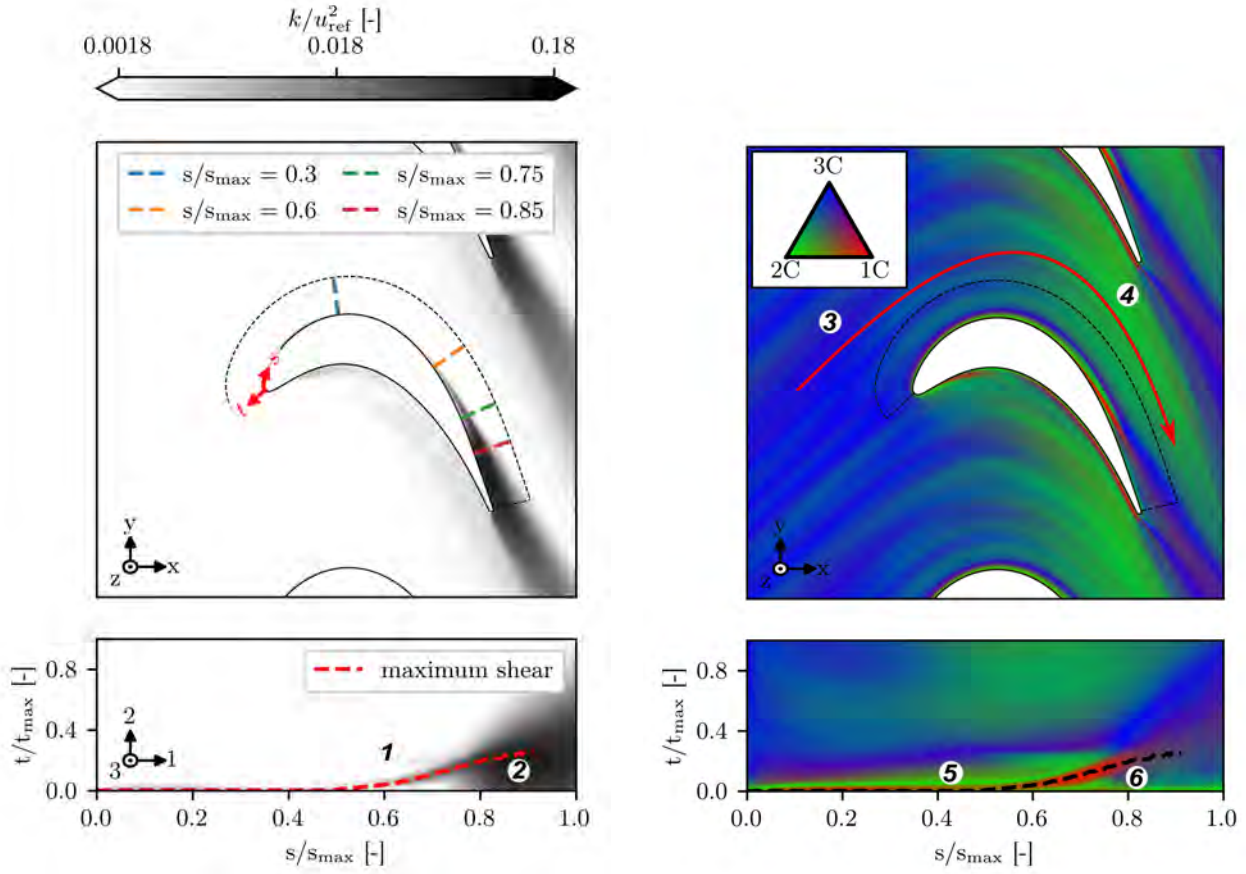

(a) Turbulent kinetic energy (logarithmic scale) **(b) Componentality of Reynolds stress anisotropy tensor**

Figure 3 Turbulence in the blade passage obtained by LES

Turbulence Anisotropy

To get a better overall understanding of the turbulence state, Figure 3b shows the componentality contours in blade-to-blade view. To do this, the methodology of Emory and Iaccarino (2014) is used, by mapping the weights C_{ic} of the barycentric map to the RGB channels. The inflow is characterized by moderate isotropic 3C incoming turbulence, which is consistent with the applied turbulent boundary conditions (region ③). In freestream, the isotropic turbulence state enters the passage until it reaches the acceleration region, promoting a shift to 2C turbulence indicated by the change from blue to green color in Figure 3b (region ④). In this region, spanwise and pitchwise fluctuations make an almost equal contribution to the turbulence level. The origin of the 2C turbulence state can be mainly traced back to the velocity gradient governing in the passage flow (Behre (2019)). Following a streamline in the middle of the passage, as shown in the Figure 3b at the top, the flow experiences a significant velocity gradient along and normal to the streamline. The high pitchwise gradient promotes the production of turbulent energy in pitchwise direction. The energy is partially redistributed to the other two components. The streamwise gradient, in an identical fashion, causes a partially redistribution to the pitchwise and spanwise component, as shown by Behre et al. (2021).

The near wall area of the profile is dominated by 1C turbulent state, in this case streamwise Reynolds stress. The 1C layer (red color) spans from near leading edge to the separation point. After the flow starts to separate, the prominent 1C turbulence state is stretched along the line, indicating the maximum shear above the reverse flow region.

The second region of interest is the 2C area directly above the 1C layer next to the wall (region ⑤). The 2C layer follows the same path as the 1C near the wall. The origin of this phenomena can be traced back to the redistribution effect of the incoming free stream 3C isotropic background turbulence at the stagnation point of the leading edge. As has been shown by Xiong and Lele (2007), the wall normal fluctuations at the stagnation point decrease close to the wall due to the non-penetration condition. The energy of the wall normal fluctuations is transferred to the other two components, creating a 2C state in the vicinity of the stagnation point. This state is convected downstream, with the mean flow tangential to the blade surface, causing the 2C layer (green color). Turbulence entrainment from the free-stream into the laminar boundary

layer patch undergoes the same redistribution of the wall-normal component, together with the turbulence damping. As a result, the 2C layer is still present along the complete laminar boundary layer part.

In the separated region ($s/s_{max} = 0.61$), the 2C turbulence is dominant close to the wall, while the turbulence away from the wall becomes isotropic. The area inside the separation bubble is characterized by 2C and 3C turbulence, with 3C turbulence being more present from $s/s_{max} = 0.8$ (region ⑥).

In summary, Figure 3b demonstrates the complexity of the investigated flow and indicates that nearly all possible states of turbulence occur in different regions of the suction side. At the same time, this explains to some extent, why most of the RANS eddy viscosity turbulence models (e.g. standard k-ω), fail to predict complex separated flows. However, the detailed characterization of the turbulence is the key element for development of appropriate RANS model extensions.

After looking at the composition of the Reynolds stress anisotropy tensor of the flow, subsequent figures illustrate relevant turbulence states in respect of the contribution of the different fluctuating components.

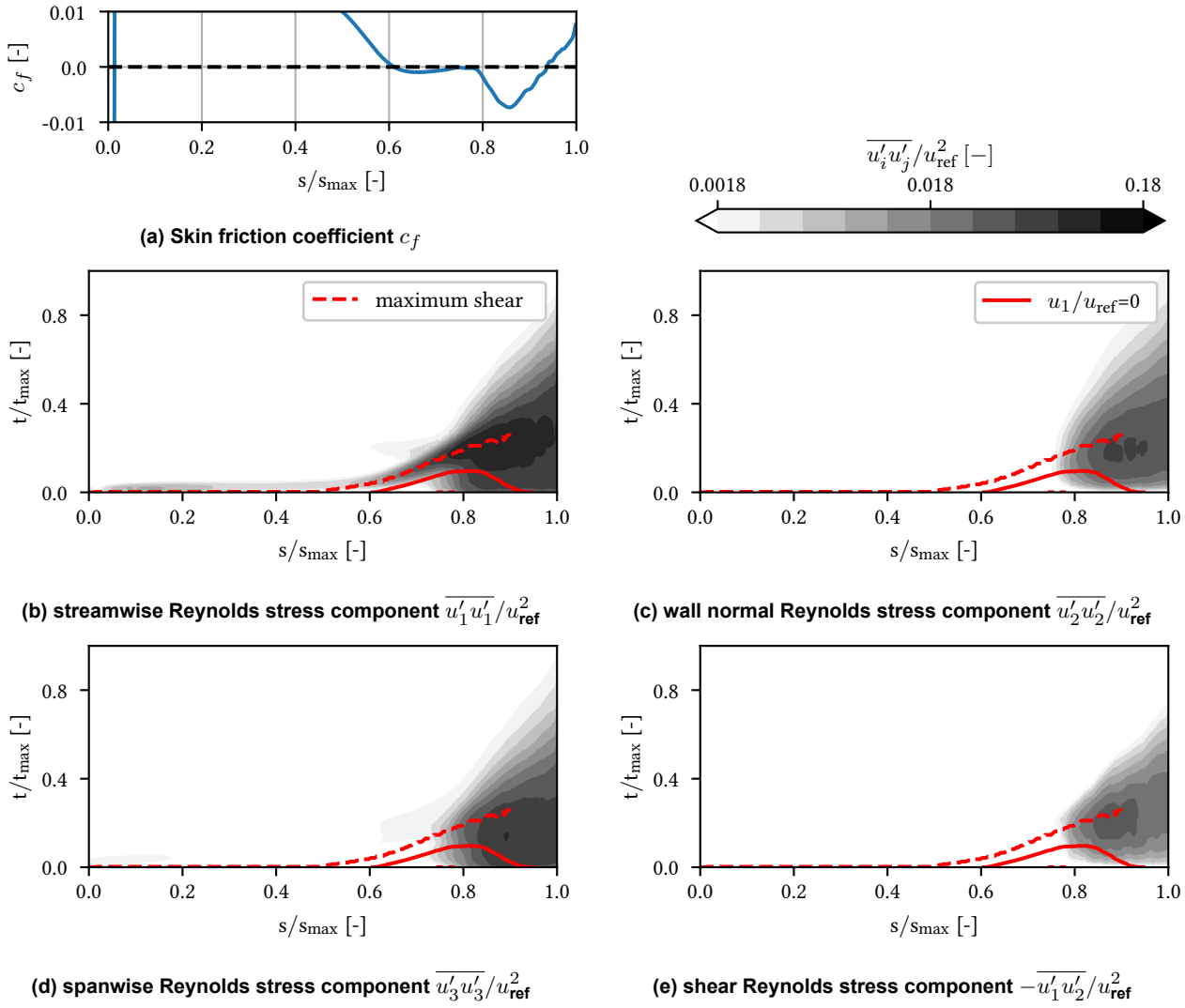

(a) Skin friction coefficient c_f

(b) streamwise Reynolds stress component $\overline{u_1' u_1'}/u_{ref}^2$

(c) wall normal Reynolds stress component $\overline{u_2' u_2'}/u_{ref}^2$

(d) spanwise Reynolds stress component $\overline{u_3' u_3'}/u_{ref}^2$

(e) shear Reynolds stress component $-\overline{u_1' u_2'}/u_{ref}^2$

Figure 4 Skin friction coefficient c_f and Reynolds stress components (with logarithmic scale) along the suction side obtained by LES

Figure 4 shows contour plots of the normal and shear Reynolds stresses, normalized by the mean outlet velocity (u_{ref}). Superimposed are the inflection line ($u_1/u_{ref} = 0$) and maximum shear line. In order to discern separation and reattachment points, the skin friction coefficient c_f - calculated on averaged statistic samples - is also plotted in Figure 4a. Following these plots, the boundary layer separates at around $s/s_{max} = 0.61$ and reattaches at around $s/s_{max} = 0.93$. This is confirmed by the skin friction coefficient, crossing zero for the first time and reaching positive values in the aft section. One should note that identifying a reattachment point or line, based on the skin friction plot, is justified for a steady laminar separation bubble. Whereas in transitional and turbulent separation bubbles, the instantaneous flow field is highly unsteady and varies continuously over time. The definition of a reattachment point could therefore be misleading. Here, the definition is based on the time-averaged velocity distribution.

Looking at the streamwise Reynolds stress component $\overline{u_1{}'u_1{}'}$ (Figure 4b), a continuous amplification along the max shear line can be observed. This reaches a maximum value of 12 % around $s/s_{max} = 0.86$, while propagating highly turbulent flow towards the wall. This effect is in line with the maximum negative value of the skin friction coefficient and high turbulent kinetic energy (Figure 3a). The high levels of the streamwise velocity stresses can be traced back to the streamwise streaks (pre-transitional Klebanoff modes) generated in the upstream laminar boundary layer. These streaks become unstable and end up generating turbulent spots in the shear layer. The streamwise component has the highest contribution among the Reynolds stress components and shows a steep growth from leading edge, which is perfectly in line with the 1C turbulence layer shown in Figure 3b.

Both wall normal $\overline{u_2{}'u_2{}'}$ and spanwise $\overline{u_3{}'u_3{}'}$ Reynolds stress components (Figure 4c and Figure 4d, respectively) are negligible upstream of the separation bubble and start to grow simultaneously, at around $s/s_{max} = 0.8$. Spanwise fluctuations are the second important contribution regarding the intensity. In the rear part of the separation bubble, the Reynolds shear stress $\overline{u_1{}'u_2{}'}$ (Figure 4e) reaches almost the same value as the wall normal Reynolds stress. This is strongly related to the amplification and saturation of the instabilities and indicates the fully turbulent state. The maximum value of fluctuations is reached where large-scale vortex shedding occurs (as a consequence of the shear layer roll-up) and represents the strength of the large-scale turbulence in moving freestream fluid towards the surface.

Wall Normal Profiles of Turbulence

After investigating the streamwise evolution of the anisotopy and Reynolds stresses, the following figures present with the Reynolds stress distribution perpendicular to the wall. As in Figure 3b, to get a better overall understanding of the turbulence state, the componentality contours are visualized by mapping the weights C_{ic} of the barycentric map to the RGB channels via the barycentric map. To this end, four relevant axial positions on the suction side surface are selected (marked lines in Figure 3a top left). Additionally, the turbulence anisotropy state is plotted as a barycentric RGB map. It should be noted that the ranges of x and y axis are plotted independently in each sub figure. This is due to a better visualization of the fluctuations in the boundary layer. Since the fluctuations and the corresponding turbulence anisotropic behavior differ considerably depending on the boundary layer state.

Starting from the front part of the suction side in Figure 5a, in which the flow accelerates and a laminar boundary layer exists, a mixture of 1C and 2C isotropic turbulence state is observed in near wall area ($y^+ < 20$). Moving further towards the outer layer of the boundary layer, the spanwise contribution becomes more prominent, moving more towards isotropic 2C turbulent state, as seen in Figure 3b. The turbulence state outside the boundary layer is governed by isotropic 3C. This pattern is maintained, after passing the suction peak (maximum of Ma_{is} on the suction side) at $s/s_{max} = 0.3$ and reaching the separation bubble at $s/s_{max} = 0.6$ (Figure 5b). There is a difference in the free-stream flow, compared to the axial positions before $s/s_{max} = 0.3$, which is the result of the passage flow acceleration (see the discussion of Figure 3b). The streamwise component shows two distinct peaks and the near wall region ($y^+ < 5$) shows a isotropic 2C manner.
The turbulence anisotropy state becomes more complex proceeding further into the separated region (Figure 5c). At this streamwise position, the streamwise fluctuation starts to grow rapidly (Figure 4). At the same time, in the region close to the wall ($y^+ < 5$), there is a 2C anisotropy state, which is not the case in the upstream laminar region of the boundary layer.
Moving further downstream (Figure 5d), all Reynolds stress components increase and reach their maximum level at $y^+ \approx 100$. In addition to the normal Reynolds stresses ($\overline{u_1{}'u_1{}'}$, $\overline{u_2{}'u_2{}'}$ and $\overline{u_3{}'u_3{}'}$), the shear stress $\overline{u_1{}'u_2{}'}$ also increases, which is a clear indication of the momentum and energy exchange between all Reynolds stress components. Equally important is the presence and influence of a detached shear layer itself. The separated boundary layer transports the turbulence above the separation bubble and results in high Reynolds shear stresses and turbulence production. This is consistent with the findings in Figure 4. Obviously, there is a lag of the shear stress component when compared to the normal components. While the normal components are present at all positions (in a different manner and amount), the shear stress component is only persent at the last position, where the transition process towards the fully turbulent state is completely finished.

Moving towards the edge of the boundary layer, the 2C turbulence becomes 1C in a thin region with dominant streamwise component, but is quickly changing to 3C state at the boundary layer edge. As mentioned before, the layer further above changes again to 2C state, due to flow acceleration and turning inside the turbine passage.

Comparison to RANS

Figure 6 demonstrates the difference in the prediction of Reynolds stress components between RANS (both LEVM and DRSM) and LES at $s/s_{max} = 0.85$. It should be noted that the plot of each numerical model is shown separately, since the fluctuations and the corresponding turbulence anisotropic behavior differ considerably depending on the boundary layer state in RANS and LES. In contrast to LES, the LEVM result in Figure 6a indicates isotropic 3C turbulence throughout the whole separation bubble. This is confirmed by similar values for normal Reynolds stresses ($\overline{u_1{}'u_1{}'} \approx \overline{u_2{}'u_2{}'} \approx \overline{u_3{}'u_3{}'}$).

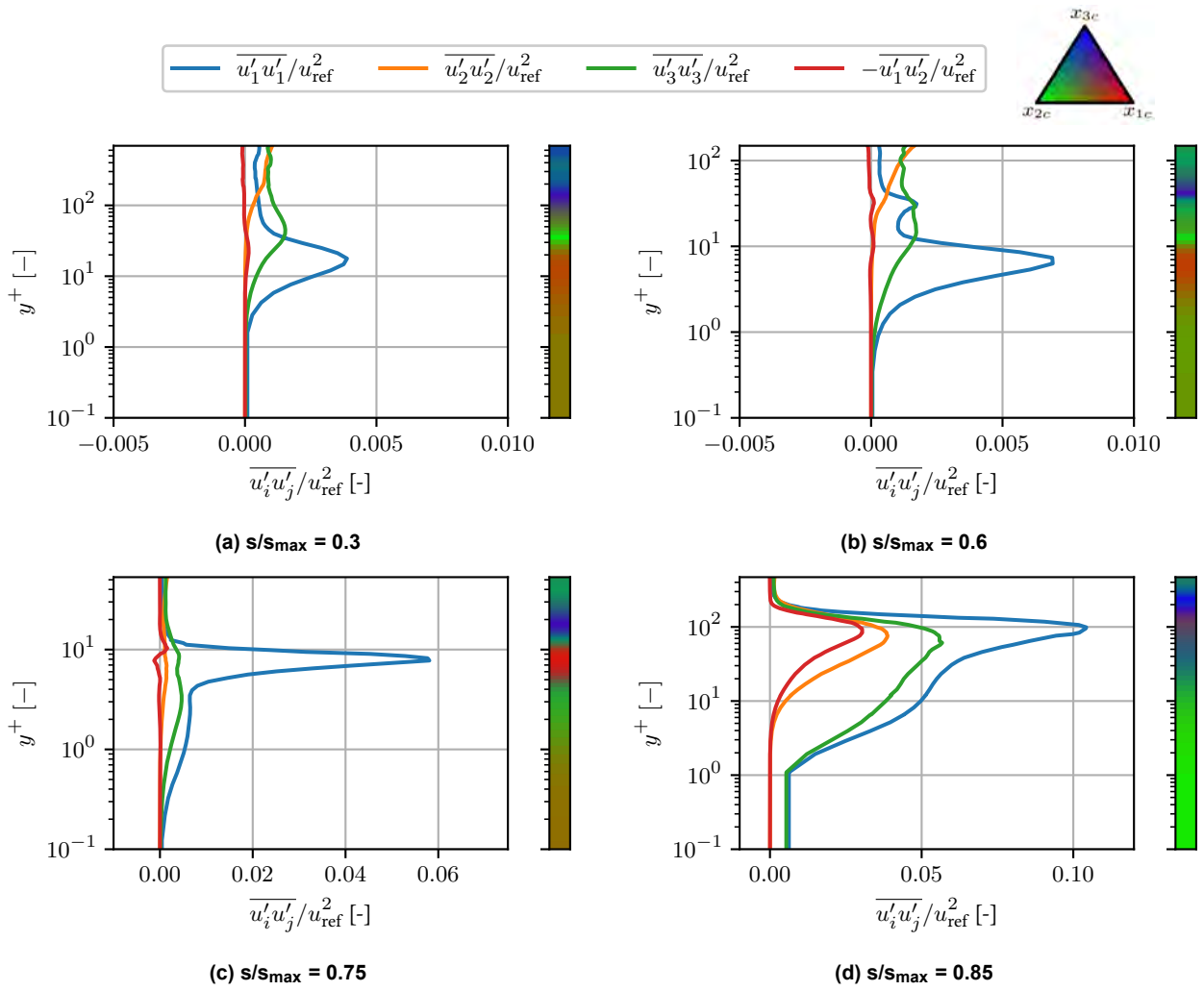

Figure 5 Reynolds stresses (lines) and the corresponding componentality of Reynolds stress anisotropy tensor (colorbars) along wall normal lines at four defined streamwise positions as in Figure 3a obtained by LES

Further, the magnitude of the LEVM predicted normal stresses and the corresponding turbulent kinetic energy is much smaller than the corresponding LES predictions. Similar results are reported by Müller-Schindewolffs et al. (2017) and Pichler et al. (2015) for such applications. Looking at the shear stress, similar behaviour can be observed for the LEVM and LES, that means the shear stress is smaller and lags behind the normal stresses.

The DRSM is able to reproduce the correct anisotropic behavior only to some extend. Especially the two component turbulence state close to the wall is not captured by the SSG/LRR-ω model. Nevertheless at $y^+ \approx 40$, the DRSM results show, unlike LEVM, a better trend regarding the Reynolds stress contributions. At this wall normal position the DRSM predicts different normal and shear Reynolds stress contributions ($\overline{u_1'u_1'} > \overline{u_3'u_3'} > \overline{u_2'u_2'}$), which resembles the distribution of LES. The magnitude of the predicted normal and shear stresses and the corresponding turbulent kinetic energy by the DRSM are weaker than predicted by LES.

The numerical results show that the underestimation of Reynolds stress is a significant factor in the unsatisfactory prediction of separation. These results emphasize the need to improve the prediction of reverse-flow speed in separation bubbles by LEVMs and DRSMs.

CONCLUSIONS

An investigation of the low-pressure turbine cascade MTU-T161 via LES with respect to the turbulence anisotropy is presented. The flow at low Reynolds number 90×10^3 shows a laminar separation bubble which undergoes transition into turbulent state and reattaches close to the trailing edge. The comparison between RANS (LEVM and DRSM) and LES with respect to isentropic Mach number distribution on the profile and total pressure loss in the wake show clear deficiencies of the RANS prediction and a very good agreement of the LES prediction to the experiments. The turbulence state in various regions on the suction side is analyzed with focus on the components of the Reynolds stress anisotropy tensor.

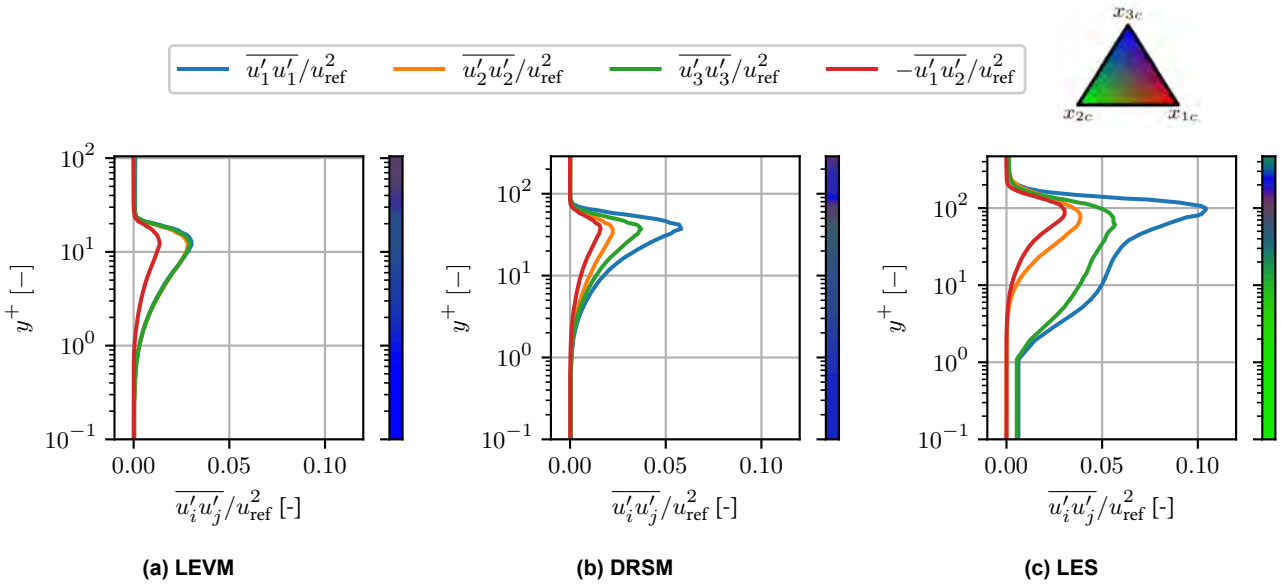

Figure 6 Comparison of Reynolds stresses (lines) and the corresponding componentality of Reynolds stress anisotropy tensor (colorbars) between (a) LEVM, (b) DRSM and (c) LES at s/s_{max}=0.85

Using the barycentric map, it can be concluded that the flow over the LPT suction side includes nearly all possible states of turbulence occurring in different regions. It can be seen that the flow near the wall is governed by one-component anisotropy state, followed by a two-component layer above. The near wall area develops the two-component turbulence within the separated region. In the final stage, the fully developed turbulent state is identified by decreasing the anisotropy in the velocity fluctuations. The separated shear layer above the separation bubble changes from two-component to one-component and subsequently to three-component state. The passage flow also undergoes a shift from three-component isotropic behavior, entering the passage, to two-component turbulence during the large acceleration and flow turning inside the turbine passage.

Finally, LEVM predictions show a nearly isotropic turulence prediction in the separation region, clearly demonstrating the inability of this approach to reproduce the strongly anisotropic turbulence characteristics. This is considered to be the main reason for poor RANS predictions of Mach number distribution and total pressure loss. DRSM results show slightly anisotrop behavior in the boundary layer and separation bubble. Nevertheless the magnitude of Reynolds stress components are still underestimated comapred to LES. The mean flow quantities in the middle section are not captured better than LEVM via DRSM. The present analysis underlines the complexity of the flow in relevant turbomachinery applications, even in two-dimensional mid-span flows. In particular, the turbulence anisotropy seems to be the key element for accurate flow predictions and reliable blade design. This aspect needs more attention in future research and development work, both in turbulence modelling and aerodynamic blade design. Such analysis provide insights for turbulence modelling community to come up with new anisotropic models or turbulence model extensions. These results show that there are still deficiencies in modeling the Reynolds stress transport equation, which need to be further analyzed and corrected so as to improve the current models. This can be done based on novel machine learning techniques.

NOMENCLATURE

Acronyms

Abbreviation	Description
CFD	Computational Fluid Dynamics
DRSM	Differential Reynolds Stress Models
EARSM	Explicit Algebraic Reynolds Stress Models
KH	Kelvin-Helmholtz
LE	Leading Edge
LES	Large Eddy Simulation
LEVM	Linear Eddy Viscosity Models
LPT	Low Pressure Turbine
RANS	Reynolds-averaged Navier-Stokes
STG	Synthetic Turbulence Generator

Abbreviation	Description
TE	Trailing Edge
TKE	Turbulent Kinetic Energy
TRACE	Turbomachinery Research Aerodynamic Computational Environment
WRLES	Wall Resolved Large Eddy Simulation

Latin symbols

Symbol	Description
a_{ij}	Reynolds Stress Anisotropy Tensor
$\overline{u_i' u_j'}$	Reynolds Stress Tensor
c_f	Skin Friction Coefficient
h	Blade Span
l	Profile Chord Length
Ma	Mach number
Ma_{is}	isentropic Mach number
Re	Reynolds number
t	Profile Pitch
Zw	Zweifel Number

Greek symbols

Symbol	Description
β_1	inflow angle
β_2	outflow angle
β_s	stager angle
Δx^+	streamsise nondimensional wall unit
Δy^+	normal nondimensional wall unit
Δz^+	spanwise nondimensional wall unit

ACKNOWLEDGMENTS

This work was funded by the Federal Ministry for Economic Affairs and Climate Action (BMWK) on the basis of a resolution of the German Federal Parliament within the framework of the Federal Aviation Research Programme under grant number 20T1719D. The authors gratefully acknowledge MTU Aero Engines for providing the MTU-T161 cascade for this study and the permission to publish the paper. Special thanks go to the German Aerospace Center (DLR) for providing the TRACE solver. Additionally, the authors gratefully acknowledge the computing time granted by the JARA allocation board and provided on the JARA partition part of the supercomputer CLAIX at RWTH Aachen University.

REFERENCES

Antonia, R. A., Djenidi, L. and Spalart, P. R. (1994), 'Anisotropy of the dissipation tensor in a turbulent boundary layer', *Physics of Fluids* **6**(7), 2475–2479.

Banerjee, S., Krahl, R., Durst, F. and Zenger, C. (2007), 'Presentation of anisotropy properties of turbulence, invariants versus eigenvalue approaches', *Journal of Turbulence* **8**, N32.

Behre, S. (2019), Instationäre Analyse turbulenter Größen in einer Axialturbine, Dissertation, RWTH Aachen.

Behre, S., Kožulović, D., Hösgen, C. and Jeschke, P. (2021), Development of turbulent quantities inside an axial turbine vane, *in* 'Proceedings of ASME Turbo Expo 2021: Turbomachinery Technical Conference and Exposition', The American Society of Mechanical Engineers, New York, N.Y.

Bergmann, M., Morsbach, C., Ashcroft, G. and Kügeler, E. (2022), 'Statistical error estimation methods for engineering-relevant quantities from scale-resolving simulations', *Journal of Turbomachinery* **144**(3).

Bode, C. (2018), Verbesserte Wiedergabe der Turbulenz in Turbinenströmungen und deren Einfluss auf das dreidimensionale Grenzschichtverhalten, Dissertation, Technische Universität Braunschweig.

Choi, K.-S. and Lumley, J. L. (2001), 'The return to isotropy of homogeneous turbulence', *Journal of Fluid Mechanics* **436**, 59–84.

Comte, F. D. P. and Lesieur, M. (1996), 'Large-eddy simulation of transition to turbulence in a boundary layer developing spatially over a flat plate', *Journal of Fluid Mechanics* **326**, 1–36.

Coull, J. D. and Hodson, H. P. (2011), 'Unsteady boundary-layer transition in low-pressure turbines', *Journal of Fluid Mechanics* **681**, 370–410.

Denton, J. D. (2010), Some limitations of turbomachinery CFD, *in* 'Proceedings of the ASME Turbo Expo 2010', ASME, New York, NY, pp. 735–745.

Eisfeld, B. and Brodersen, O. (2005), Advanced turbulence modelling and stress analysis for the dlr-f6 configuration, *in* '23rd AIAA Applied Aerodynamics Conference', p. 4727.

Eisfeld, B., Rumsey, C. and Togiti, V. (2016), 'Verification and validation of a second-moment-closure model', *AIAA Journal* **54**(5), 1524–1541.

Emory, M. and Iaccarino, G. (2014), Visualizing turbulence anisotropy in the spatial domain with componentality contours, Annual research briefs 2014, Center for Turbulence Research, Stanford University, Stanford, CA, USA.

Entlesberger, R.-G., Martinstetter, M. and Staudacher, W. (2005), Untersuchungen am Turbinengitter T161 zur Bestimmung der Profildruckverteilung und der Gittercharakteristik, Institutsbericht LRT-WE12-05/02, Universität der Bundeswehr München, Neubiberg, Germany.

Fischer, M., Jovanović, J. and Durst, F. (2001), 'Reynolds number effects in the near-wall region of turbulent channel flows', *Physics of Fluids* **13**(6), 1755–1767.

Gier, J., Franke, M., Hübner, N. and Schröder, T. (2010), 'Designing low pressure turbines for optimized airfoil lift', *Journal of Turbomachinery* **132**(3), 436.

Gier, J. and Hübner, N. (2005), Design and analysis of a high stage loading five-stage lp turbine rig employing improved transition modeling, *in* 'Volume 6: Turbo Expo 2005, Parts A and B', ASMEDC, pp. 759–769.

Huai, X., Joslin, R. D. and Piomelli, U. (1997), 'Large-eddy simulation of transition to turbulence in boundary layers', *Theoretical and Computational Fluid Dynamics* **9**(2), 149–163.

Kato, M. and Launder, B. E. (1993), The modelling of turbulent flow around stationary and virbrating square cylinders, *in* F. Durst, N. Kasagi, B. E. Launder, F. W. Schmidt, K. Suzuki and J. H. Whitelaw, eds, '9th Symposium on Turbulent Shear Flows', Springer Berlin Heidelberg, Berlin, Heidelberg, pp. 10.4.1–10.4.6.

Krogstad, P.-Å. and Torbergsen, L. E. (2000), 'Invariant analysis of turbulent pipe flow', *Flow, Turbulence and Combustion* **64**(3), 161–181.

Langtry, R. B. and Menter, F. R. (2009), 'Correlation-based transition modeling for unstructured parallelized computational fluid dynamics codes', *AIAA Journal* **47**(12), 2894–2906.

Launder, B. E., Reece, G. J. and Rodi, W. (1975), 'Progress in the development of a reynolds-stress turbulence closure', *Journal of fluid mechanics* **68**(3), 537–566.

Leyh, S. and Morsbach, C. (2020), The coupling of a synthetic turbulence generator with turbomachinery boundary conditions, *in* M. García-Villalba, ed., 'Direct and Large Eddy Simulation XII', Vol. 27 of *ERCOFTAC Ser*, Springer International Publishing AG, Cham, pp. 349–355.

Lumley, J. L. (1979), Computational modeling of turbulent flows, *in* 'Advances in Applied Mechanics Volume 18', Vol. 18 of *Advances in Applied Mechanics*, Elsevier, pp. 123–176.

Menter, F. R. (1994), 'Two-equation eddy-viscosity turbulence models for engineering applications', *AIAA Journal* **32**(8), 1598–1605.

Morsbach, C. (2017), Reynolds Stress Modelling for Turbomachinery Flow Applications, Dissertation.

Morsbach, C. and Bergmann, M. (2020), Critical analysis of the numerical setup for the large-eddy simulation of the low-pressure turbine profile t106c, *in* M. García-Villalba, ed., 'Direct and Large Eddy Simulation XII', Vol. 27 of *ERCOFTAC Ser*, Springer International Publishing AG, Cham, pp. 343–348.

Müller-Schindewolffs, C., Baier, R.-D., Seume, J. R. and Herbst, F. (2017), 'Direct numerical simulation based analysis of rans predictions of a low-pressure turbine cascade', *Journal of Turbomachinery* **139**(8).

Nicoud, F. and Ducros, F. (1999), 'Subgrid-scale stress modelling based on the square of the velocity gradient tensor', *Flow, Turbulence and Combustion* **62**(3), 183–200.

Pichler, R., Sandberg, R. D., Michelassi, V. and Bhaskaran, R. (2015), Investigation of the accuracy of rans models to predict the flow through a low-pressure turbine, *in* 'Proceedings of the ASME Turbo Expo: Turbine Technical Conference and Exposition - 2015', ASME, New York, NY.

Rist, U., Lang, M. and Wagner, S. (2004), 'Investigations on controlled transition development in a laminar separation bubble by means of lda and piv', *Experiments in Fluids* **36**(1), 43–52.

Roberts, S. K. and Yaras, M. I. (2003), Effects of periodic unsteadiness, free-stream turbulence, and flow reynolds number on separation-bubble transition, *in* 'Proceedings of the ASME Turbo Expo 2003', American Society of Mechanical Engineers, New York, NY, pp. 745–759.

Roe, P. (1981), 'Approximate riemann solvers, parameter vectors, and difference schemes', *Journal of Computational Physics* **43**(2), 357–372.

Sandberg, R. D. and Michelassi, V. (2019), 'The current state of high-fidelity simulations for main gas path turbomachinery components and their industrial impact', *Flow, Turbulence and Combustion* **102**(4), 797–848.

Schenck, T. and Jovanović, J. (2002), 'Measurement of the instantaneous velocity gradients in plane and axisymmetric turbulent wake flows', *Journal of Fluids Engineering* **124**(1), 143–153.

Schlüß, D., Frey, C. and Ashcroft, G. (2016), Consistent non-reflecting boundary conditions for both steady and unsteady flow simulations in turbomachinery applications, *in* M. Papadrakakis, ed., 'Proceedings of the VII European Congress on Computational Methods in Applied Sciences and Engineering (ECCOMAS Congress 2016)', Institute of Structural Analysis and Antiseismic Research School of Civil Engineering National Technical University of Athens (NTUA) Greece, Athens, pp. 7403–7422.

Shur, M. L., Spalart, P. R., Strelets, M. K. and Travin, A. K. (2014), 'Synthetic turbulence generators for rans-les interfaces in zonal simulations of aerodynamic and aeroacoustic problems', *Flow, Turbulence and Combustion* **93**(1), 63–92.

Speziale, C. G., Sarkar, S. and Gatski, T. B. (1991), 'Modelling the pressure–strain correlation of turbulence: an invariant dynamical systems approach', *Journal of fluid mechanics* **227**, 245–272.

Tucker, P. G. (2014), *Unsteady Computational Fluid Dynamics in Aeronautics*, Vol. 104 of *SpringerLink Bücher*, Springer, Dordrecht.

Tyacke, J. C. and Tucker, P. G. (2015), 'Future use of large eddy simulation in aero–engines', *Journal of Turbomachinery* **137**(8).

van Leer, B. (1979), 'Towards the ultimate conservative difference scheme. v. a second-order sequel to godunov's method', *Journal of Computational Physics* **32**(1), 101–136.

Volino, R. J. (2010), 'Separated flow measurements on a highly loaded low-pressure turbine airfoil', *Journal of Turbomachinery* **132**(1).

Wilcox, D. C. (1988), 'Reassessment of the scale-determining equation for advanced turbulence models', *AIAA Journal* **26**(11), 1299–1310.

Xiong, Z. and Lele, S. K. (2007), 'Stagnation-point flow under free-stream turbulence', *Journal of Fluid Mechanics* **590**, 1–33.

Yan, H., Liu, Y. and Lu, L. (2019), 'Turbulence anisotropy analysis in a highly loaded linear compressor cascade', *Aerospace Science and Technology* **91**(3), 241–254.

Yang, Z. (2011), Large eddy simulation of a transition process in separated-reattached flows, *in* C. A. Brebbia and G. M. Carlomagno, eds, 'Computational Methods and Experimental Measurements XV', WIT Transactions on Modelling and Simulation, WIT PressSouthampton, UK, pp. 181–192.